Sensors & Actuators: A. Physical 340 (2022) 113536

Contents lists available at ScienceDirect

Sensors and Actuators: A. Physical

journal homepage: www.journals.elsevier.com/sensors-and-actuators-a-physical

A flexible dipole antenna for direct transduction of microwave radiated power into DC mechanical deflection

R. Ruiz *, J. Bonache, G. Abadal

Departament d'Enginyeria Electrònica, Universitat Autònoma de Barcelona, Bellaterra 08193, Spain

ARTICLE INFO

Keywords:
RF-MEMS
Wireless power transfer
Electrostatic actuation

ABSTRACT

A new device resulting from the merging of mechanical and electromagnetic properties of a couple of conductive cantilevered beams is described in this paper. The device, which is based on two metallic clamped-free beams which, at the same time, are the arms of a radio frequency dipole antenna is capable to receive the electromagnetic power radiated from an emitting antenna and transduce it directly in a dc mechanical actuation. A numerical model developed to describe the behavior of the device has been validated through the test of a millimeter scale demonstrator working in the microwave frequency band.

1. Introduction

Multidisciplinary nature of microelectromechanical systems technology (MEMS) has been proved along its recent history, through its impact on mature disciplines as optics, biology or microwave engineering, giving rise to new application areas such as MOEMS [1], Bio-MEMS [2] or RF-MEMS [3]. In particular, works involving switching networks [4], low noise oscillators [5], amplifiers [6], tunable capacitors [7] and reconfigurable antennas [8] have been extensively reported in the field of RF-MEMS. To excite and detect static displacements or dynamic vibrations of suspended moving elements, transducing mechanisms in RF-MEMS involve, in most of the cases, electrostatic actuation and detection through optimized comb-drive [9,10] or parallel plate [11,12] capacitive structures that are integrated using MEMS technologies.

Concerning driving and biasing of the MEMS capacitive structures, controlled voltage signals as well as dc bias voltages that can be externally applied, are preferably synthesized by on-chip integrated circuitry [13], using hybrid technologies as CMOS-MEMS [14]. Thus, although low dc voltages are always needed as power supply of the active CMOS circuitry [15], large bias voltages are usually required not only as driving signal [16,17], but also to generate detectable currents in the readout capacitive MEMS structures [18]. Therefore, capacitive MEMS devices are intrinsically active since they need a dc voltage to work. However, one of the main drawbacks of electrostatic transduction is imposed by the pull-in instability, which comes from the need to polarize the structures. It is well known that when a simple voltage source is used to drive the structure, its range of displacement is limited to around 1/3 of the capacitive transduction gap [19]. Several strategies based on a current source driving [20], a high frequency actuation [21], a series capacitor [22], or a levitation base electrode [23] have proved to overcome this limitation.

Resonant driving [24–27] is a very promising alternative to extend the operation range, which is based on using an LC circuit resonator to drive the electrostatic actuator. In this case, the frequency dependence of the ac driving voltage introduces useful negative feedback that compensates the pull-in instability. But, as an additional advantage, resonant driving operated at the resonance frequency of the LC circuit allows to get an amplifying effect on the ac driving voltage, which allows to consequently lower the excitation ac voltage.

In the work reported here we present a new concept derived from the resonant driving strategy that makes possible to drive a capacitive MEMS structure without any on-chip locally applied voltage. The new concept, called direct transduction from electromagnetic to mechanical domain is sustained by a new device called MEMSTENNA. Such a MEMSTENNA, which is a combination of an electrostatic MEMS capacitive transducer and a radio frequency antenna, consists of two clamped-free metal beams that constitute, at the same time, the two arms of a dipole antenna. The free ends of both beams are separated along an overlapping short length, so that a parallel plate capacitive transducer is defined between both arms of the antenna. When an electromagnetic radiation is received by the MEMSTENNA, an ac voltage is generated in its feed point, i.e. the capacitive MEMS transducer in this case, so that the induced ac electrostatic force will produce a flexural actuation on both flexible arms of the MEMSTENNA. In the present work we describe a numerical model of the MEMSTENNA

* Corresponding author.

https://doi.org/10.1016/j.sna.2022.113536
Received 25 November 2021; Received in revised form 7 March 2022; Accepted 29 March 2022
Available online 13 April 2022

device, and we discuss the test results of a proof-of-concept prototype designed and fabricated to validate the model.

Potential applications of a MEMSTENNA are foreseen as the core structure of a batteryless and wireless relay in, for instance, wake up wireless circuits [28] which have promising applications in IoT technologies [29]. Here, the MEMSTENNA could be configured in a relay structure that can be switched ON and OFF by a remote RF power control pulse. Unlike standard wake up wireless solutions, a MEMSTENNA based relay would not only be activated remotely but it would also be powered remotely since the mechanical switching function would be not only controlled but also powered wirelessly. However, as it will be discussed later in this paper, the RF power levels needed to mechanically actuate our actual MEMSTENNA proof-of-concept demonstrators are too high to be realistic for a practical application, and hence an optimization of the power efficiency of the MEMSTENNA device is mandatory for the success of future applications.

2. Working principle and modelization of the device

As described in Fig. 1, the MEMSTENNA device is composed of two metal arms of dimensions L, w and t (length, width and thickness), which is, from an electromagnetic perspective, a half-wavelength dipole receiver antenna [30] with a modified feeding point. The referred modification consists of placing the antenna arms in parallel along a certain overlapping length, l_m, and separated by a gap distance, g_0. Thereby, the standard feeding port of the antenna is converted into an electrostatic MEMS actuator defined by the MEMS capacitor, C_m, which plates area is $A=l_m \cdot w$, and distance between plates is g_0. On the other hand, the mentioned two arms are, at the same time and from a mechanical point of view, two clamped-free beams (cantilevers) having the free end at the modified feeding point converted to the electrostatic actuator and the anchors at the opposite end. Thus, when the MEMSTENNA is receiving an electromagnetic wave, an ac voltage is induced at the modified feeding point and the electrostatic attractive force induced in the MEMS capacitor will produce a deflection of both clamped-free beams. Notice that since the frequency of the microwave radiation, typically in the GHz range, is usually orders of magnitude larger than the resonance frequency of the beams (Hz-kHz), any vibration can be excited directly on the cantilevers. However, because of the nonlinear dependence of the electrostatic force with its inducing voltage (it is proportional to V^2), a dc component on the force is present and a static deflection of the beams is produced.

To modelize the behavior of the MEMSTENNA, let us consider linearly polarized incident electromagnetic plane waves propagating in the z-direction with the electric field, E_{inc}, aligned along the longitudinal direction of the antenna, x-axis, as shown in Fig. 1.c. As the dipole works in the receiving mode, when an electromagnetic wave excites the antenna, a voltage, V_m, is generated at the antenna gap, i.e, the MEMS capacitive actuator. Consequently, an electrostatic force, F_{ee}, is applied in the z-direction at each of the plates of the MEMS capacitor producing the mutual attraction of the cantilevers at its very end.

The MEMSTENNA, as a receiving antenna, is electrically modeled by its Thévenin equivalent circuit [31,32], which, as shown in the left side of Fig. 2, is defined by a series antenna's impedance, Z(ω), given by:

$$Z(\omega) = R_a(\omega) + jX_a(\omega) = R_a(\omega) + j\omega L_a - j\frac{1}{\omega C_a} \quad (1)$$

and an open-circuit voltage, V_{OC}, that can be calculated [33] from the effective length, L_{eff}, and the incident electric field, E_{inc}, as:

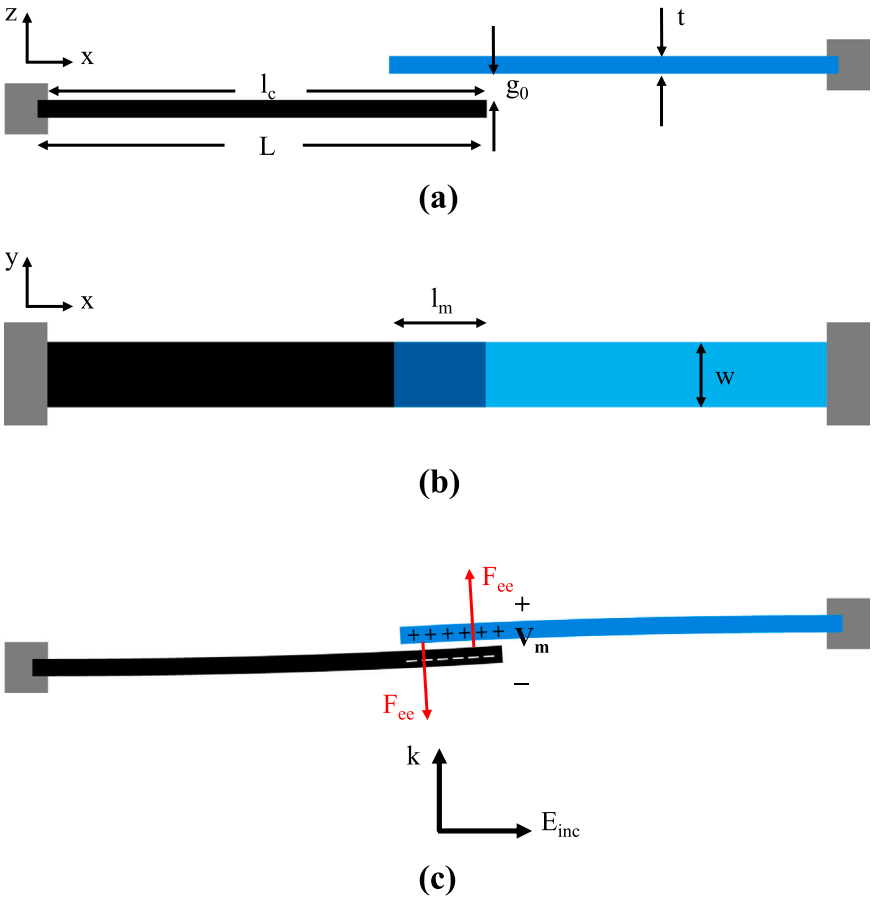

Fig. 1. Lateral (a) and top (b) views of the MEMSTENNA structure based on a dipole antenna structure, with arms being mechanical beams in a clamped-free configuration. (c) Bending of the MEMSTENNA beam components produced by the electrostatic force, F_{ee}.

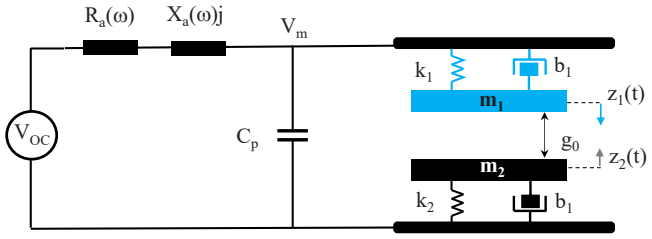

Fig. 2. Thévenin equivalent circuit of the MEMSTENNA as a dipole antenna (left side) loaded by the MEMS capacitive actuator (right side), represented by its spring-mass-damper model.

$$V_{OC} = L_{eff} \cdot E_{inc} \tag{2}$$

The effective length, L_{eff}, for a half-wavelength dipole is defined in [33], where a uniform and sinusoidal current distribution of the dipole is considered. Therefore, an average value of $2/\pi = 0.64$ for the maximum sinusoidal current distribution has been considered. As the length of the antenna component of our MEMSTENNA device is $L = \lambda/2$, the effective length is given by:

$$L_{eff} = 0.64 \cdot L \tag{3}$$

Additionally, right side of Fig. 2 shows the electromechanical model of the MEMS capacitive actuator, which is based on a pair of spring-mass-damper systems, associated to the double cantilever components of the MEMSTENNA. Eqs. (4) and (5) describe the dynamic behavior of the top and bottom cantilevers, respectively.

$$m_1 \cdot \frac{d^2 z_1(t)}{dt^2} + b_1 \cdot \frac{dz_1(t)}{dt} + k_1 \cdot z_1(t) = F_{ee} \tag{4}$$

$$m_2 \cdot \frac{d^2 z_2(t)}{dt^2} + b_2 \cdot \frac{dz_2(t)}{dt} + k_2 \cdot z_2(t) = F_{ee} \tag{5}$$

Here, F_{ee} represents the electrostatic force, m_1 and m_2 are the effective masses of each beam component, k_1 and k_2 are their spring constants and b_1 and b_2 are the damping factors. The time-dependent deflections of each beam at their very end are represented by $z_1(t)$ and $z_2(t)$. C_p is a parasitic capacitance which is in parallel with the active MEMS capacitor, C_m, and V_m is the voltage induced in the feeding point of the MEMSTENNA which, as pointed out above, corresponds to the actuation voltage applied at the MEMS capacitive actuator terminals.

The electrostatic force F_{ee} acting on each component of the double cantilever system is defined as:

$$F_{ee} = \frac{\epsilon_0 \cdot A \cdot V_m^2}{2 \cdot (g_0 - z_1(t) - z_2(t))^2} \tag{6}$$

If we consider each component of the double cantilever as identical, then Eqs. (4), (5) and (6) can be reduced to a single equation as:

$$m \cdot \frac{d^2 z(t)}{dt^2} + b \cdot \frac{dz(t)}{dt} + k \cdot z(t) = \frac{\epsilon_0 \cdot A \cdot V_m^2}{2 \cdot (g_0 - 2 \cdot z(t))^2} \tag{7}$$

Finally, Fig. 3 shows the block diagram of the model implementation. In a first block, the movement equation of the cantilevers (Eq. 7) is numerically solved and the time evolution of the cantilevers deflection, z (t), is obtained. In the second block, the MEMS capacitance, that changes when the cantilevers move, $C_m(z(t))$, is calculated taking z(t) as an input. Also in this block, the antenna impedance components, R_a and X_a, are calculated by means of the method of moments (MoM) [34]. From the antenna and the MEMS capacitance impedances, the voltage at the MEMS capacitive actuator terminals, V_m, is determined. Then, to close the loop, the electrostatic force, F_{ee}, is calculated in the third block, as of the cantilevers deflection, z(t), and the MEMS actuator voltage, V_m.

3. Test results of a proof-of-concept demonstrator. Model validation

3.1. Prototype description

A MEMSTENNA demonstrator has been fabricated as a proof-of-concept prototype to experimentally validate the model described in Section 2. The main characteristics of the prototype have been summarized in Table 1.

As predicted by the model, the MEMSTENNA dipole impedance shows a resonance frequency around 800 MHz, corresponding to a null of the reactance (Fig. 4.a). Below this frequency the antenna behavior is capacitive ($X_a(f<800\ MHz) \approx R_a + (1/j \cdot \omega \cdot C_a)$), and it is inductive for higher frequencies ($X_a(f>800\ MHz) \approx R_a + j \cdot \omega \cdot L_a$). However, as it is shown in Fig. 4.b, the capacitive load C_m of the MEMS is modifying the original antenna reactance, X_a, producing an increase of the resonant frequency of the dipole antenna when the gap is increasingly opening.

3.2. Measurement setup description

The measurement set up is depicted in Fig. 5. On the transmission

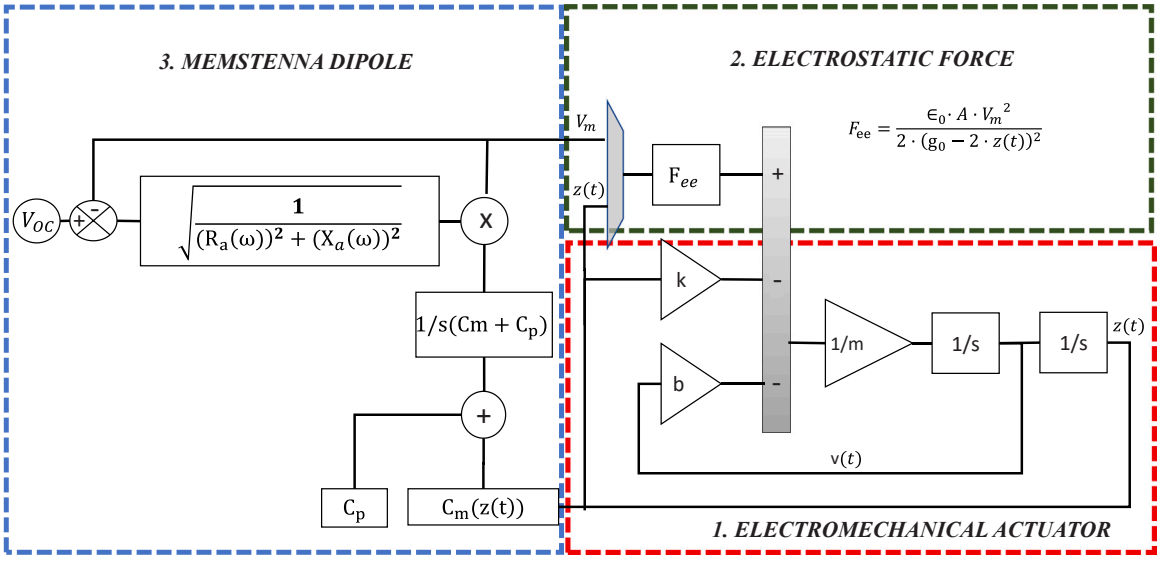

Fig. 3. Block diagram of the MEMSTENNA model.

Table 1
Physical parameters of the MEMSTENNA proof-of-concept prototype.

Parameter	Symbol	Value	units
Density (Steel)	ρ	8050	kg/m^3
Young Modulus (Steel)	E	200	GPa
Length of the cantilever Length of the dipole	l_c/L	83/88	mm
Width	w	5	mm
Overlapping length	l_m	803	μm
Thickness	t	100	μm
Static gap	g_o	50	μm
Spring constant	k	0,43	mN/m
Frequency of the 1st cantilever mode	f_0	6,8	Hz
Frequency of the 1st dipole antenna mode(for g_o=50 μm)	f_a	875	MHz

side, an RF signal generator (HP 8647 A) followed by a RF 12 W power amplifier (RFPA RF101000–10) is connected to a λ/2 dipole emitting antenna designed to resonate at 940 MHz. The generator and power amplifier set can deliver a RF power slightly above 12 W to the emitting antenna, which radiates a carrier signal (the above-mentioned excitation electromagnetic wave) of frequency f_c. The MEMSTENNA, aligned in the x-axis, is placed at a certain distance from the emitter dipole. The anchors of both MENTENNA's cantilevers are attached to xyz micropositioners to allow a fine adjustment of the MEMSTENNA gap, g_o, and overlap length, l_m. A diode laser beam (635 nm, 1.2 mW) is focused on the back side of the top cantilever and the deflection angle of the reflected beam is measured by a Position Sensitive Device (PSD) (New Focus 2930). The vertical displacement of the top cantilever free end, represented by z_2 in Fig. 5, is consequently measured through an oscilloscope (Tektronix MDO3024) connected to the PSD output. A zenithal CCD camera is placed on top of the MEMSTENNA in the capacitive transduction zone to optically adjust the gap distance. In this set up we are considering that the two arms of the MEMSTENNA have the same displacement ($z_1 = z_2$), and the RF incident wave is plane. To have a control of the excitation electric field through the signal generator, we have measured the electric field intensity at the memstenna position for different signal generator powers using an electric field probe.

3.3. Test results and discussion

3.3.1. Switching transient response

In a first set of measurements, we have analyzed the time response during OFF-ON and ON-OFF switching transients at different excitation electric fields and gap values for a fixed carrier frequency (f_c=834 MHz). As it is shown in Fig. 6, the cantilever response presents a small overshoot in both OFF-ON and ON-OFF transients that is almost mixed up with the mechanical noise fluctuations observed along the stationary states. On the other hand, the average stationary vertical deflection achieved after OFF-ON switching transient grows when the electric field is increased. In particular, when the cantilevers are separated by a gap of $g_0 = 54$ μm (Fig. 6.a) the excitation electric field can be increased up to 200 V/m before the collapse between both structures, which occurs when the MEMSTENNA is excited at 210 V/m, as it is evidenced by the dramatic reduction of the noise fluctuations in the ON stationary state. When the gap distance is increased to $g_0 = 67$ μm (Fig. 6.b), excitation electric field can be increased up to 230 V/m and the structure is not collapsed.

3.3.2. Stationary response dependence on the electric field

To precisely account for the dependence of the stationary vertical deflection on the electric field, we have collected the data shown in Fig. 7. Here, the experimental data have been fit by calculated curves from the model. In the model calculations best fit is obtained when $C_p = 0.8 \cdot C_o$. As it can be noticed, a good agreement between the experimental points and the values predicted by the model is obtained. Thus, the collapse effect observed at $g_0 = 54$ μm that has been described previously is more clearly reproduced here. Besides, it can be observed that a smooth linear dependence of the stationary vertical deflection on the electric field is reproduced for large gap values (g_0 =100 μm and g_0 =140 μm). However, such a linear dependence turns into a saturation trend when gap values (g_0 =67 μm) are reduced close to the collapse conditions (g_0 =54 μm). This dependence, which seems to be inconsistent with the square power dependence of the electrostatic force with the voltage (Eq. 6) and, consequently, with the electric field (Eq. 2), can be partly explained by the saturation of the RF power amplifier. Added to this amplifier saturation effect, an intrinsic negative feedback effect due to the increase of the capacitive load is also present here and will be analyzed below.

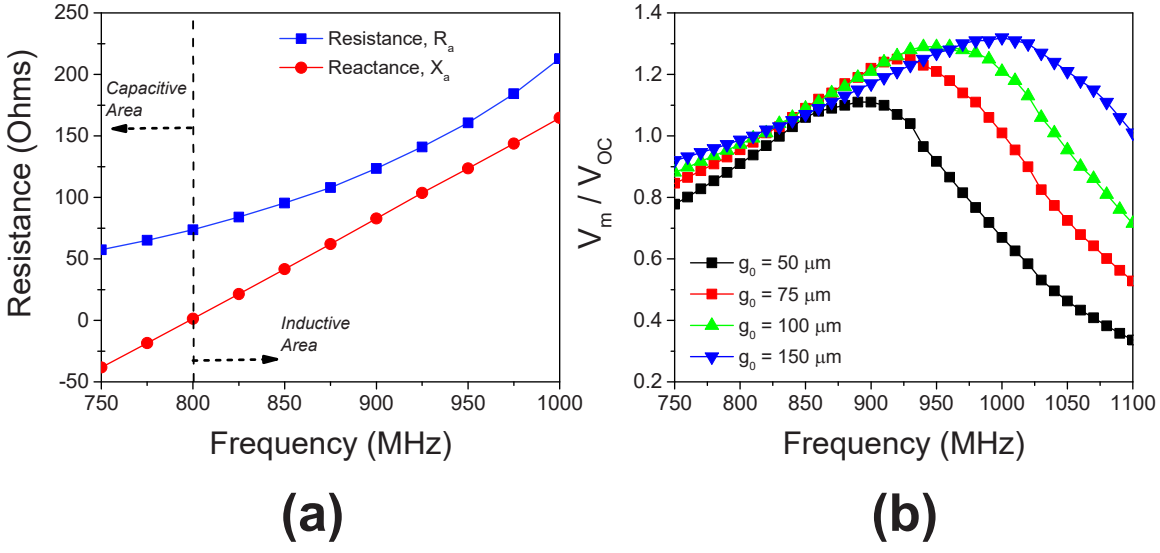

Fig. 4. Frequency response of the MEMSTENNA dipole impedance (a) and MEMS actuator voltage at different static transducing gaps for a constant electric field excitation of E_{inc}= 190 V/m (b). A parasitic parallel capacitance value of $C_p = 0.7 \cdot C_o$ is considered in the calculations.

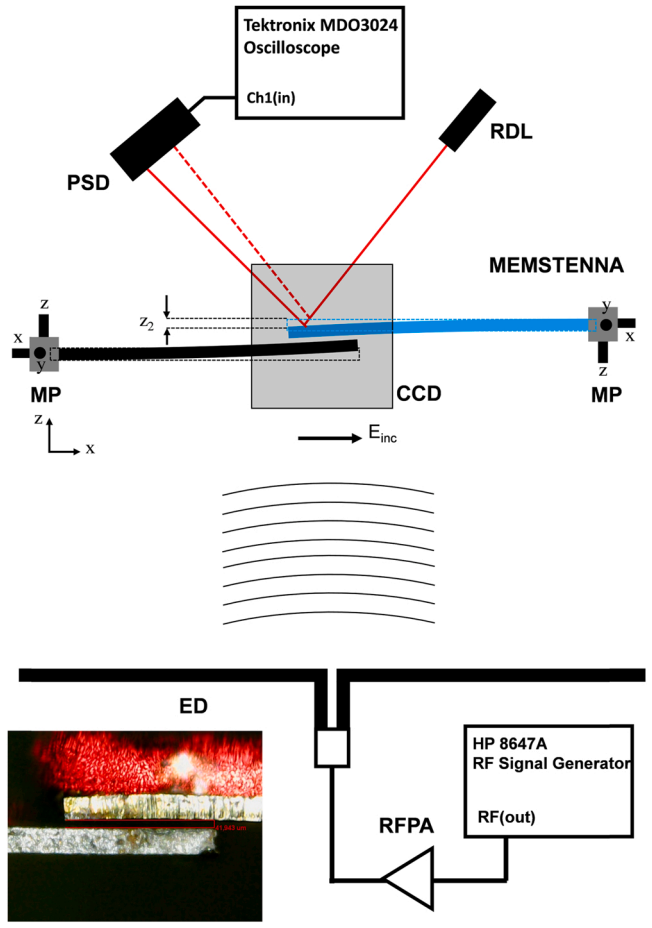

Fig. 5. Block diagram of the measurement setup. Used components: CCD: Digital camera, PSD: Position Sensitive Device, RFPA: RF Power Amplifier (12 W), ED: Emitter Dipole, RDL: Red Diode Laser ($\lambda = 673.8$ nm), MP: xyz Micro Positioner. *Inset*: Optical image of the capacitive transduction area of the MEMSTENNA with a gap $g_0 = 42$ μm.

3.3.3. Effect of the carrier frequency on the stationary response vs. carrier power dependence

To bring out clearly the effect described in previous section, we have calculated how the stationary vertical deflection grows with the electric field intensity for different carrier frequencies and for an initial gap $g_0 = 50$ μm, using the model equations. The resulting curves are plotted in Fig. 8. For carrier frequencies below the resonance frequency of the MEMSTENNA dipole (see Table 1), i.e. $f_c < 875$ MHz (see Fig. 4.b), the cantilever collapses almost like when driven by a voltage source and the collapse position is close to $g_0/3 = 16.7$ μm (see dashed curves in Fig. 8, corresponding to 0.7–0.85 GHz). In fact, collapse is produced earlier because when load capacitance is increased by the gap reduction, then resonance frequency of the MEMSTENNA dipole is shifted down ($f_{res}=1/(L{\cdot}C)^{1/2}$) and, consequently, the amplitude of the driving voltage V_m, grows, inducing an extra positive feedback effect, that allows collapsing the structure by exciting with lower electric field values. Indeed, the

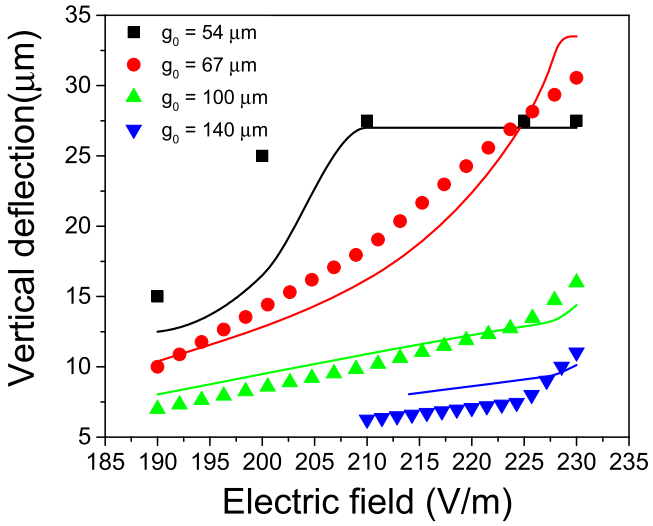

Fig. 7. Experimental (symbol points) and calculated (solid curves) stationary response of the MEMSTENNA as a function of the electric field at the memstenna, for different gap values at a constant carrier frequency of $f_c = 834$ MHz. Best fit is obtained when $C_p = 0.8{\cdot}C_o$.

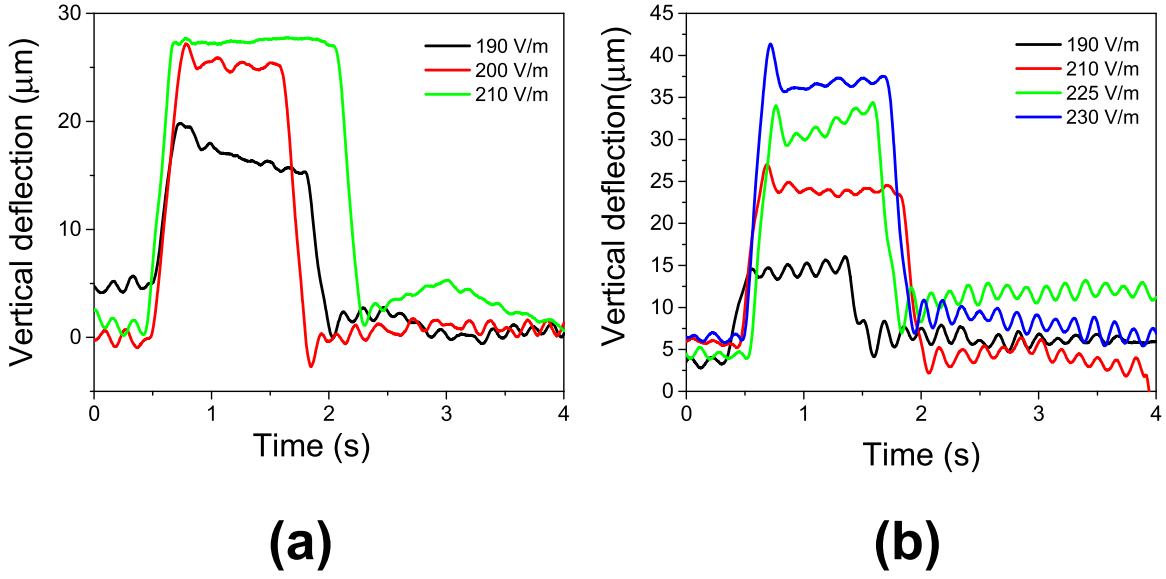

Fig. 6. Time evolution of the vertical deflection of the top cantilever during OFF-ON and ON-OFF switching transients for $g_0 = 54$ μm (a) and $g_0 = 67$ μm (b), and different excitation electric field values. Carrier frequency is kept constant at $f_c = 834$ MHz.

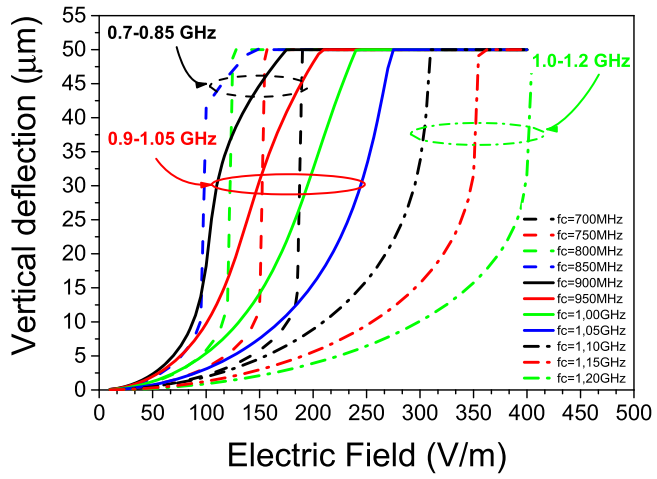

Fig. 8. Calculated stationary vertical deflection of the MEMSTENNA as a function of the incident electric field for different carrier frequencies. The gap is kept constant at $g_0 = 50$ µm.

higher the carrier frequency of the dashed curves in Fig. 8 (0–7–0.85 GHz), the lower the electric field needed for the structure to collapse. Instead, the opposite feedback effect is produced when the starting point corresponds to a carrier frequency above the resonance frequency of the MEMSTENNA dipole, i.e. $f_c > 875$ MHz (see Fig. 4.b). In this case, the amplitude of the driving voltage V_m, decreases as the gap is closing and the collapse instability can even be avoided (see solid curves in Fig. 8, corresponding to 0.9–1.05 GHz), as reported previously in the literature [25]. Finally, when the carrier frequency is far above the resonance frequency of the MEMSTENNA, i.e., $f_c > 1.05$ GHz, the previous negative feedback effect is increasingly reduced, so that the collapse of the structures is produced again at a gap position which is also increasingly reduced as the carrier frequency is increased (see dashed-point curves in Fig. 8, corresponding to 1.0–1.2 GHz).

A sample of some of the model predicted curves shown in Fig. 8 have been experimentally reproduced and shown in Fig. 9. The measured points and model fit curves obtained at carrier frequencies $f_c = 820$ MHz and $f_c = 845$ MHz corresponds to the final part of the positive feedback regime (dashed curves in Fig. 8, 0.7–0.85 GHz). A reduction of the collapse electric field is clearly obtained when carrier frequency is increased from 820 MHz to 845 MHz. However, when the excitation is produced by a carrier signal with a frequency (f_c=950 MHz) inside the negative feedback regime, the electric field needed to actuate the structure is increased and the collapse is practically cancelled, as the sigmoidal shape curve like the ones predicted by the model (solid curves in Fig. 8, 0.9–1.05 GHz) demonstrates.

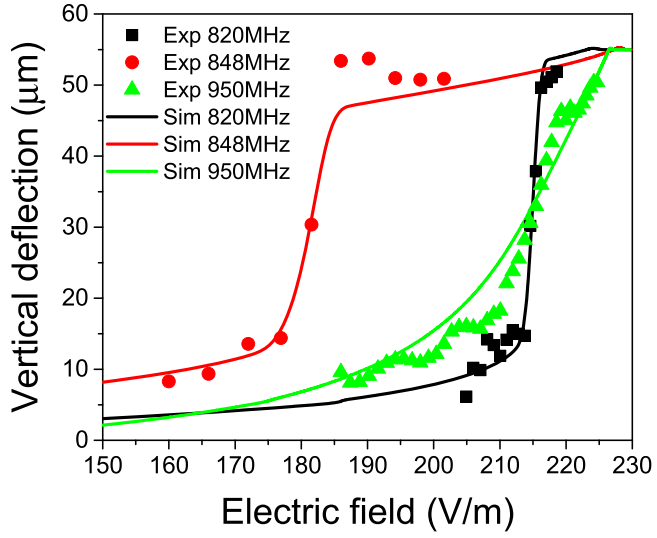

Fig. 9. Measured stationary vertical deflection of the MEMSTENNA as a function of the electric field and the corresponding model fit curves for three different carrier frequencies. The gap is kept constant at $g_0 = 110$ µm. Best fit is obtained when $C_p = 0.7 \cdot C_o$.

Considering the analyzed test results from the perspective of the above-mentioned wireless-batteryless relay future application, power efficiency can be optimized by adjusting the transduction gap and the carrier frequency into the positive feedback regime (0.7–0.85 GHz for the demonstrator case), so that the collapse of the structure occurs with the minimum electric field (or carrier power). Specifically, our test results show that collapse is produced at 210 V/m (Figs. 6 and 7) for $g_0 = 54$ µm and fc= 834 MHz or at 185 V/m (Fig. 9) for $g_0 = 110$ µm and fc= 848 MHz. These electric field values are obtained with carrier powers above 12 W and 7 W, respectively. Even in the best case predicted by the model (Fig. 8, $g_0 = 50$ µm, fc=700 MHz) the electric field needed to collapse is around 100 V/m, which is obtained with a carrier power of 1.25 W in our setup conditions. An additional improvement that would allow to further decrease the carrier power below 1 W or, alternatively, to increase the distance between the MEMSTENNA and the emitter dipole antenna, can be achieved by downscaling the MEMSTENNA dimensions. Indeed, a dimensional analysis shows that if we downscale all the geometric dimensions of the MEMSTENNA by a scale factor SF, the collapse voltage

$$V_{collapse} = \sqrt{\frac{k \cdot g_0^3}{\epsilon_0 \cdot A}} \tag{8}$$

will also scale linearly with SF, since spring constant, $k = 0.25 \cdot E \cdot w \cdot (t/l_c)^3$, scales like SF, g_0^3 scales like SF^3 and transduction area, A, scales like SF^2. On the other hand, the transduction voltage, which is proportional to the open circuit voltage, V_{OC} (Eq. 2) scales like SF too. This means that when we downscale the whole structure, the voltage needed to collapse, $V_{collapse}$, is reduced, but the available voltage is reduced too. Consequently, a solution could consist of reducing the length of the MEMSTENNA by a scale factor smaller than the scale factor of the rest of dimensions, so that the collapse voltage is reduced more than the open circuit voltage.

4. Conclusions

The concept of MEMSTENNA has been defined and described in terms of structure, configuration and working principle, which is based on the resonant driving phenomenology associated to the LC of MEMSTENNA dipole antenna. A complete model of the MEMSTENNA that includes the electromagnetics of the dipole antenna and its mutual interaction with the mechanics of the cantilevers components has been also described. A mm-scale proof-of-concept prototype of MEMSTENNA made of steel has been fabricated to validate the model. Its geometry has been designed in such a way that the dipole antenna associated to the prototype resonates at 875 MHz and the cantilever components have a spring constant of 0.43 mN/m, corresponding to a mechanical fundamental mode resonance of 6.8 Hz. Both, transient and stationary measurements of the cantilever's deflection have been performed at different transduction gap, carrier frequency and electric field conditions. In particular, the two experimental characteristics families corresponding to cantilever deflection vs. electric field, parametrized by the transduction gap and carrier frequency, have been contrasted to the calculated curves obtained from model calculations. The degree of agreement between theoretical curves and experimental points allows to successfully validate the MEMSTENNA model.

Declaration of Competing Interest

The authors declare that they have no known competing financial interests or personal relationships that could have appeared to influence the work reported in this paper.

Acknowledgements

We would like to acknowledge the group collaborators of Prof. Jordi Bonache for their unvaluable help in the antenna modelization. We would also like to acknowledge financial support by Spain's Ministerio de Ciencia, Innovación y Universidades under Grant No. RTI2018-097876-B-C21 (MCIU/AEI/FEDER, UE).

References

[1] S. Boutami, B.B. Bakir, J.L. Leclercq, X. Letartre, C. Seassal, P. Rojo-Romeo, P. Viktorovitch, Photonic crystal-based MOEMS devices, IEEE J. Sel. Top. Quantum Electron. 13 (2) (2007) 244–252.
[2] B. Ziaie, A. Baldi, M. Lei, Y. Gu, R.A. Siegel, Hard and soft micromachining for BioMEMS: review of techniques and examples of applications in microfluidics and drug delivery, Adv. Drug Deliv. Rev. 56 (2) (2004) 145–172.
[3] J.J. Yao, RF MEMS from a device perspective, J. Micromech. Microeng. 10 (4) (2000) R9.
[4] G.M. Rebeiz, K. Entesari, I.C. Reines, S.J. Park, M.A. El-Tanani, A. Grichener, A. R. Brown, Tuning in to RF MEMS, IEEE Microw. Mag. 10 (6) (2009) 55–72.
[5] W.T. Hsu, Vibrating RF MEMS for timing and frequency references. In 2006 IEEE MTT-S International Microwave Symposium Digest. 2006, June, pp. 672–675). IEEE.
[6] R. Malmqvist, P. Rantakari, C. Samuelsson, M. Lahti, S. Cheng, J. Saijets, J. Varis, RF MEMS based impedance matching networks for tunable multi-band microwave low noise amplifiers, Int. Semicond. Conf. 1 (2009) 303–306.
[7] T.G. Rijks, J.T. M. Van Beek, P.G. Steeneken, M.J. E. Ulenaers, J. De Coster, R. Puers . RF MEMS tunable capacitors with large tuning ratio. In 17th IEEE International Conference on Micro Electro Mechanical Systems. Maastricht MEMS 2004 Technical Digest. 2004, January, pp. 777–780. IEEE.
[8] A. Pourziad, S. Nikmehr, H. Veladi, A novel multi-state integrated RF MEMS switch for reconfigurable antennas applications, Prog Electromagn. Res. 139 (2013) 389–406.
[9] D. Hah, S.Y. Huang, J.C. Tsai, H. Toshiyoshi, M.C. Wu, Low-voltage, large-scan angle MEMS analog micromirror arrays with hidden vertical comb-drive actuators, J. Micro Syst. 13 (2) (2004) 279–289.
[10] S. Kavitha, R.J. Daniel, K. Sumangala, Design and analysis of MEMS comb drive capacitive accelerometer for SHM and seismic applications, Measurement 93 (2016) 327–339.
[11] C.H. Han, D.H. Choi, J.B. Yoon, Parallel-plate MEMS variable capacitor with superior linearity and large tuning ratio using a levering structure, J. Microelectromech. Syst. 20 (6) (2011) 1345–1354.
[12] G.N. Nielson, G. Barbastathis, Dynamic pull-in of parallel-plate and torsional electrostatic MEMS actuators, J. Microelectromech. Syst. 15 (4) (2006) 811–821.
[13] J. Wang, J. Yang, D. Chen, L. Jin, Y. Li, Y. Zhang, F. Wu, Gas detection microsystem with MEMS gas sensor and integrated circuit, IEEE Sens. J. 18 (16) (2018) 6765–6773.
[14] H. Baltes, O. Brand, A. Hierlemann, D.A.L.D. Lange, C.A.H.C. Hagleitner. CMOS MEMS-present and future. In Technical Digest. MEMS 2002 IEEE International Conference. Fifteenth IEEE International Conference on Micro Electro Mechanical Systems (Cat. No. 02CH37266), 2002, January, pp. 459–466.
[15] J. Verd, A. Uranga, J. Segura, N. Barniol. A 3V CMOS-MEMS oscillator in 0.35 μm CMOS technology. In 2013 Transducers & Eurosensors XXVII: The 17th International Conference on Solid-State Sensors, Actuators and Microsystems (TRANSDUCERS & EUROSENSORS XXVII). 2013 (pp. 806–809). IEEE.
[16] M. Pallay, R.N. Miles, S. Towfighian, Towards a high bias voltage MEMS filter using electrostatic levitation, Mech. Syst. Signal Process. 150 (2021), 107250.
[17] J.B. Muldavin, G.M. Rebeiz, Inline capacitive and DC-contact MEMS shunt switches, IEEE Microw. Wirel. Compon. Lett. 11 (8) (2001) 334–336.
[18] H. Yang J.S. Cho Y. Yang S. Kim. A load variation tolerant readout interface for high linear MEMS capacitive microphones. In 2017 IEEE international symposium on circuits and systems (ISCAS). 2017, May (pp. 1–4). IEEE.
[19] W.M. Zhang, H. Yan, Z.K. Peng, G. Meng, Electrostatic pull-in instability in MEMS/NEMS: a review, Sens. Actuators A Phys. 214 (2014) 187–218.
[20] L. Castañer, J. Pons, R. Nadal-Guardia, A. Rodrıguez, Analysis of the extended operation range of electrostatic actuators by current-pulse drive, Sens. Actuators A Phys. 90 (3) (2001) 181–190.
[21] F. Lakrad, M. Belhaq, Suppression of pull-in instability in MEMS using a high-frequency actuation, Commun. Nonlinear Sci. Numer. Simul. 15 (11) (2010) 3640–3646.
[22] E.K. Chan, R.W. Dutton, Electrostatic micromechanical actuator with extended range of travel, J. Micro Syst. 9 (3) (2000) 321–328.
[23] M. Ozdogan, S. Towfighian, R.N. Miles, Modeling and characterization of a pull-in free MEMS microphone, IEEE Sens. J. 20 (12) (2020) 6314–6323.
[24] S. Park, E. Abdel-Rahman, Low voltage electrostatic actuation and displacement measurement through resonant drive circuit. International Design Engineering Technical Conferences and Computers and Information in Engineering Conference, American Society of Mechanical Engineers, 2012, pp. 119–126.
[25] J.M. Kyynäräinen, A.S. Oja, H. Seppä, Increasing the dynamic range of a micromechanical moving-plate capacitor, Analog Integr. Circuits Signal Process. 29 (1) (2001) 61–70.
[26] S. Park, Y. Bai, J.T. Yeow. Design and analysis of resonant drive circuit for electrostatic actuators. In 2010 International Symposium on Optomechatronic Technologies. 2010, October) (pp. 1–6). IEEE.
[27] B. Cagdaser, B.E. Boser. Resonant drive for stabilizing parallel-plate actuators beyond the pull-in point. In The 13th International Conference on Solid-State Sensors, Actuators and Microsystems, 2005. Digest of Technical Papers. TRANSDUCERS'05. 2005, June, (Vol. 1, pp. 688–692). IEEE.
[28] F. Hutu, A. Khoumeri, G. Villemaud, J.M. Gorce, 2014, January. Wake-up radio architecture for home wireless networks. In 2014 IEEE Radio and Wireless Symposium (RWS) (pp. 256–258). IEEE.
[29] A. Frøytlog, L.R. Cenkeramaddi. Design and implementation of an ultra-low power wake-up radio for wireless IoT devices. In 2018 IEEE International Conference on Advanced Networks and Telecommunications Systems (ANTS). 2018 Dec 16, (pp. 1–4). IEEE.
[30] Balanis, C.A., Antenna theory (analysis and design), WILLEY INTERSCIENCE, 2005, ISBN: 0–471-66782-X.
[31] S.R. Best, B.C. Kaanta, A tutorial on the receiving and scattering properties of antennas, IEEE Antennas Propag. Mag. 51 (5) (2009) 26–37.
[32] R.P. Meys, A summary of the transmitting and receiving properties of antennas, IEEE Antennas Propag. Mag. 42 (3) (2000) 49–53.
[33] J.D. Kraus, Antennas for All Applications, McCraw-Hill, New York, 1997, pp. 254–256.
[34] S.N. Makarov, V. Iyer, S. Kulkarni, S.R. Best, Antenna and EM Modeling with MATLAB Antenna Toolbox, John Wiley & Sons, 2021.

Raul Ruiz received his M.S in Electronic Engineering in 2000 from the Universitat Autònoma de Barcelona. He has more than 18 years of experience in tasks of design and verification of ASIC. At present he works at EKRAN SYSTEMS as ASIC/SoC consulting engineer. His research interests include design, characterization and integration of micro and nanoelectromechanical systems (MEMS and NEMS). He is currently developing his PhD in MEMS direct transduction from electromagnetic to mechanical domain.

Dr. Gabriel Abadal received his degree in physics in 1991 and his PhD in electrical engineering in 1997 from the UAB. Since 2002 he is an Associate Professor in the Electronics Engineering Department of the UAB, where he currently leads the NANERG LAB group (http://grupsderecerca.uab.cat/nanerglab/). During the last 28 years he has participated in more than 30 national and European research projects, he has contributed to more than 160 conferences and he has published more than 80 papers in journals (H-index: 21). Since 2006, he focused his activity in the application of MOEMS and NOEMS to harvest energy from ambient vibrations and electromagnetic radiation sources at the nanoscale. His actual interest is oriented towards the study of graphene and other 2D materials as basic components of the future nanoenergy harvesting strategies.

Dr. Jordi Bonache was born in Cardona (Barcelona), Spain, in 1976. He received the Physics and Electronics Engineering degrees and the Ph.D. in electronics engineering from the Universitat Autònoma de Barcelona, in 1999, 2001 and 2007, respectively. In 2000, he joined the High Energy Physics Institute of Barcelona, where he was involved in the design and implementation of the control and monitoring system of the MAGIC telescope. In 2001, he joined the Department of Electronics Engineering, Universitat Autònoma de Barcelona, where he is currently Professor of Electronics. From 2006–2009, he was the Executive Manager of CIMITEC, Bellaterra, Spain. His current research interests include active and passive microwave devices, metamaterials, antennas and RFID.